CHAPTER

2

Literature review

Introduction

In 1834, the polymeric derivative known as "melon" was first synthesized and named by Liebig et al. This compound, characterized by its intriguing chemical structure, sparked further investigation into its derivatives and their properties.

One significant advancement came through the work of Franklin, who delved into the structural intricacies of melon derivatives. His experiments revealed that heating melon with thiocyanate led to the formation of carbon nitrides, specifically identified as C_3N_4. These carbon nitrides exhibited a unique graphite-like structure, distinct from the typical properties associated with melon itself.

The discovery of carbon nitrides from melon derivatives marked a pivotal moment in the understanding of polymeric compounds and their chemical transformations. Franklin's findings provided crucial insights into the reactivity and structural versatility of melon derivatives under specific thermal conditions, highlighting their potential applications in materials science and organic chemistry.

Moreover, the formation of C_3N_4 from melon and thiocyanate underscored the complexity of polymeric systems and their capacity to yield novel molecular structures

with potentially valuable properties. This discovery not only expanded the theoretical framework of polymeric chemistry but also contributed to advancements in synthetic methodologies aimed at designing and manipulating molecular architectures for various industrial and technological purposes.

Furthermore, Franklin's investigation exemplified the interdisciplinary nature of chemical research, integrating principles of organic chemistry, materials science, and physical chemistry to elucidate the behaviour of polymeric compounds under controlled experimental conditions. By elucidating the formation of carbon nitrides from melon derivatives, Franklin's work paved the way for further exploration into the synthesis and applications of polymeric materials with tailored properties and functionalities.

In conclusion, the synthesis of "melon" in 1834 and Franklin's subsequent discovery of carbon nitrides derived from melon derivatives represented significant milestones in the evolution of polymeric chemistry, offering new perspectives on the structural diversity and transformative capabilities of polymeric compounds in scientific and industrial contexts. Figure 2.1 (Franklin, 1922) illustrated the scheme for g–C_3N_4 synthesis. Moreover, Redemann and Lucas (Rademann & Lucas, 1940) provided additional evidence that the structure of melon was influenced by the hydrogen content and manufacturing procedures, indicating that it was most likely a polymeric blend with various configurations. In 1985, Cohen proposed that g–C_3N_4 could rival diamond in hardness, sparking interest among material scientists. Since Wang's initial attempts in 1997 to synthesize g–C_3N_4, significant milestones followed: in 2006, g–C_3N_4 catalyzed Friedel–Crafts reactions for the first time (Goettmann et al., 2006), and in 2009, it became the first photo-catalyst to produce hydrogen from water under visible light (Wang X. et al., 2009). Since then, g–C_3N_4 has gained prominence due to its affordability and

straightforward synthesis, solidifying its status as a material of considerable potential (Mamba & Mishra, 2016). According to the Web of Science Core Collection, graphitic carbon nitride has been mentioned in over 9500 papers since 1971. Recently, materials based on this material have become more and more common.

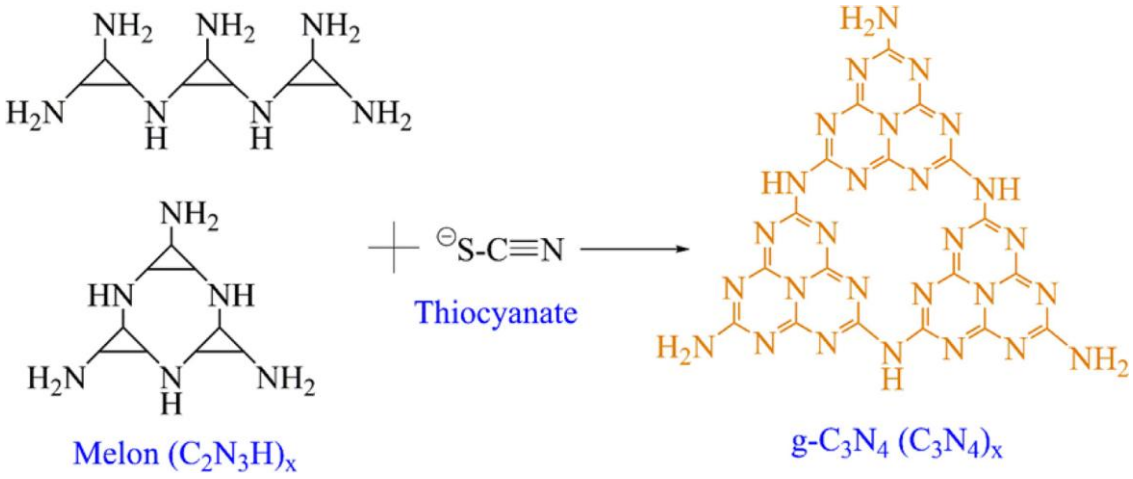

Figure 2.1. Preparation of g–C_3N_4 by pyrolysis of melon and thiocyanate (Wang and Wang, 2022).

g–C_3N_4, a metal-free 2D p-conjugated polymer, has garnered attention for its optical properties (Wen J. et al., 2017) and photocatalytic activity (Ong W., 2016). These materials also hold promise for applications including membranes, adsorbents, disinfectants, and Fenton-like catalysts (Zheng et al., 2012). Additionally, a variety of methods for altering g–C_3N_4 have been investigated in an effort to improve its functionality (Thomas et. al., 2008).

Although g–C_3N_4 has been the focus of many review papers (Jiang et. al., 2017), the majority of them were centered on photocatalytic activity and g–C_3N_4 modification. For example, Zhou et al. (Zhou et. al., 2018) gave a summary of the modifications and applications of g–C_3N_4 in photocatalysis and biosensing. Lau and Lotsch collated information on the structure properties and dimensionality–dependent photo (electro) properties of g–C_3N_4 as well as its applications in energy conversion and storage (Z. Yang

et. al. 2015). Beyond its primary role as a photo-catalyst, g–C_3N_4 has received limited attention for other environmental applications, including its use as Fenton-like reactions catalyst and characterization techniques. To advance the understanding of g–C_3N_4 synthesis, modification, and characterization, and to provide essential insights for developing highly efficient and cost-effective g–C_3N_4-based catalysts, a comprehensive review of current advancements is essential. Such a review would encompass the state of the art in synthesis methods, modifications, characterization techniques, and applications in environment field of g–C_3N_4-based materials, thereby contributing valuable knowledge to the field and facilitating further research and development in this promising area.

This chapter will critically assess recent advancements in g–C_3N_4-based materials, encompassing their synthesis, modification, and environmental applications, aiming to enhance comprehension of current developments in the field.

Setting up and determining elements making g–C_3N_4

To produce g–C_3N_4, precursors such as urea, thio–urea, cyanamide, dicyandiamide, and melamine can be thermally polymerized. The synthesis of g–C_3N_4 involves two main processes: polyaddition and polycondensation. These two processes are both impacted by temperature. Melamine is created by the precursors polymerizing, which starts the polyaddition process. After that, melamine condenses as a result of ammonia loss (polycondensation), which finally produces g–C_3N_4 polymer.

The surface area, pore volume, and grain size of g–C_3N_4 can all have a significant effect on its physiochemical properties. Many pyrolysis–based preparation methods have been developed to alter the physiochemical characteristics.

2.1 Templating methods

The aforementioned preparation strategies have been thoroughly addressed in prior research. There are two sorts of templating techniques: soft and rigid. The types of hard and soft templates might be adjusted to regulate the morphology and pore structure of g–C_3N_4.

The creation of g–C_3N_4 involved the use of organic templates, such as surfactant and amphiphilic polymer, due to soft templating techniques. These templates may cluster in the interfacial locations, influencing the inorganic phase formation in the vicinity. Figure 2.2A shows the soft templating method's scheme.

When g–C_3N_4 is synthesized utilizing hard templating procedures, stiff templates like silica and alumina oxide are utilized. First, the precursor solution is perfused into the template's mesopores. In the fixed pore channels, g–C_3N_4 would arise as a result of the stiff templates' fixed architecture. g–C_3N_4 can be obtained when the hard template is removed. Figure 2.2B depicts the hard templating method's approach. It has been discovered that g–C_3N_4's catalytic activity may be altered by the stiff template's structure. When compared to a normal silica template, g–C_3N_4 produced with silica nanostructure displayed better catalytic activity (J. Sun et. al., 2012). Removing the excess carbon from the organic template and the hard template is the last step needed for both the soft and hard templating processes. However, in the case of soft templating, residual carbon might still be present after the penultimate step, which might have an impact on the g–C_3N_4's catalytic activity. Strong acids, such hydrogen fluoride, are often needed for the final step in hard templating methods in order to remove the template, which could cause the pore structure to collapse. Furthermore, powerful acid solutions require further treatment since concentrated acids pose a harm to the environment. Wang generated porous g–C_3N_4 using

calcium carbonate particles as the hard template, which could be rapidly removed with diluted hydrochloric acid, obviating the requirement for strong acids (Wang et. al., 2015)

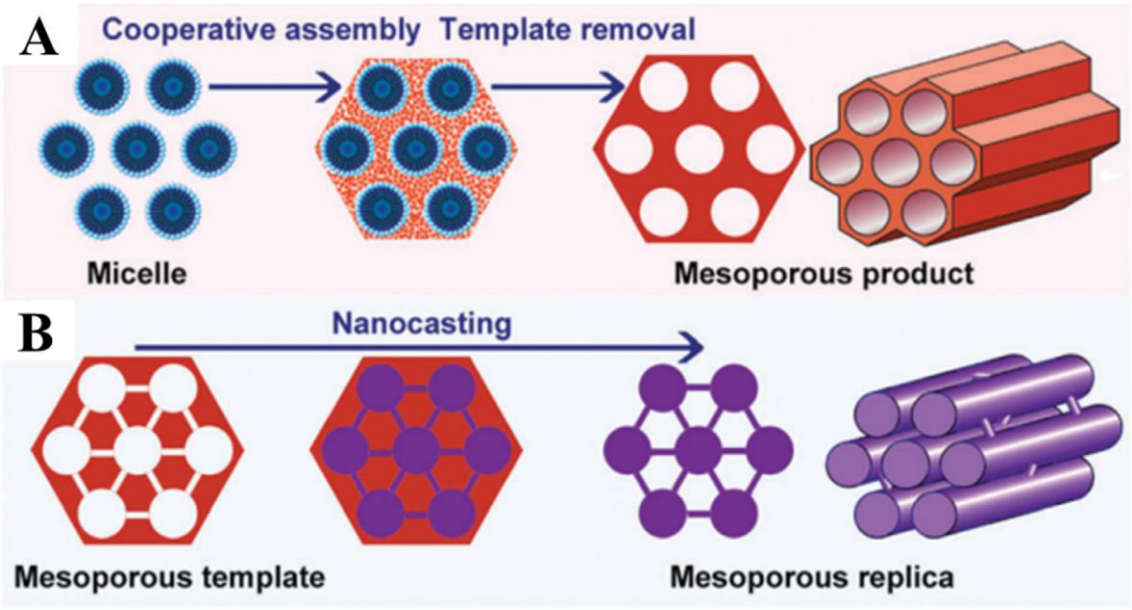

Figure 2.2. The scheme of soft templating method (A) and hard templating method (B) (Shi et al. 2011).

2.2 Template–free methods

Template-free methods offer advantages over templating methods by eliminating the need for hazardous agents like hydrofluoric acid used to remove templates such as silica matrices. Typically, g–C_3N_4 can be synthesized via pyrolysis of precursors without any additives. Post-synthesis treatments can alter the morphology of g–C_3N_4 significantly. For example, reflux techniques involving exfoliation, regrowth processes, and rolling can transform g–C_3N_4 from nanoplates to nanorods (X. Bai et al., 2013). Infrared heating of precursors of dicyandiamide also yields g–C_3N_4 without additives (Han et al., 2015), while a method combining freeze-drying assembly and hydrothermal treatment followed by thermal calcination produces seaweed-like g–C_3N_4 (Gu et al., 2015). These approaches

demonstrate diverse pathways to tailor the morphology of g–C_3N_4 through innovative synthesis methods, highlighting their versatility and potential for various applications.

2.3 Sol–gel methods

g–C_3N_4 could also be prepared by the sol–gel method, in which g–C_3N_4 precursor mixed with silica precursor or silica sol (H. Li et. al., 2016). Similar to the hard template method, the sol–gel method requires a step for template removal. In contrast to the hard template method, the silica template is created during the g–C_3N_4 preparation process as opposed to being synthesized beforehand.

2.4 Exfoliation method

One prominent technique for altering the physiochemical properties of g–C_3N_4 is exfoliation. The prepared g–C_3N_4 revealed a layer–stacked structure in the majority of cases. It has been proven that g–C_3N_4's catalytic activity can be boosted by de–laminating it into a few layers. Thermal calcination, ultrasonication, oxidative etching, and the combination of thermal calcination and ultrasonication are popular exfoliation processes. The second pyrolysis of the obtained g–C_3N_4 is referred to as thermal calcination. It can proceed with or without the presence of other substances. Without employing any chemicals, Papalias et al. (2018) accomplished a thermal exfoliation of g–C_3N_4. The thermal exfoliation of g–C_3N_4 in the presence of NH_4Cl was reported by Xu et al. (2014). The hydrothermal reaction was employed in the first stage to intercalate NH_4Cl into the g–C_3N_4 interlayers at 180°C. After that, pyrolysis was utilized to remove the NH_4^+ intercalation at 350ºC.

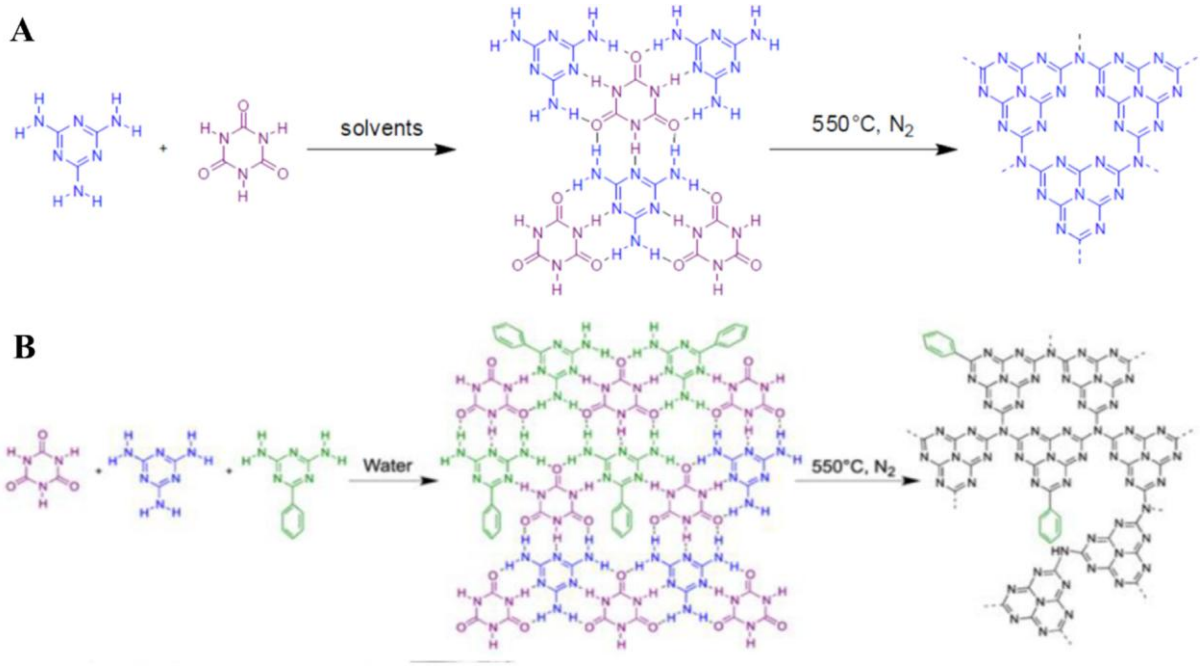

Figure 2.3. Supramolecular Preassembly Method for g–C_3N_4 Synthesis The synthesis of g–C_3N_4 involves two approaches: (Shalom et al 2013) and (Ishida et al 2014)
(A) Using cyanuric acid and melamine.
(B) Employing cyanuric acid, melamine, and 2,4–diamino–6–phenyl–1,3,5–triazine

Graphitic carbon nitride (g-C_3N_4) nanosheets are obtained through a process of exfoliation using ultra-sonication, exploiting the acoustic energy of ultrasonic waves. This method is facilitated by the weak van der Waals forces present between the layers of g-C_3N_4, facilitating their separation. Among various solvents investigated—water, ethanol, isopropanol, N-methyl-pyrrolidone, and acetone—water emerges as particularly advantageous due to its ease of post-treatment compared to other solvents.

Zhang and colleagues pioneered the use of water as a solvent for liquid exfoliation of g-C_3N_4, demonstrating precise control over the resulting physicochemical properties. Through a combination of ultra-sonication and successive centrifugation steps, they successfully produced crystalline g-C_3N_4 nanosheets. These nanosheets exhibited enhanced photocatalytic performance in hydrogen evolution. Zhang et al. (2015) achieved delamination of g-C_3N_4 into nanosheets with a thickness of approximately 2.5 nm,

corresponding to around seven C-N layers. Additionally, oxidation etching using acids (such as H_2SO_2) and alkalis (such as NaOH) contributes to g-C_3N_4 delamination. Concentrated H_2SO_4 (usually exceeding 75%) can intercalate into the interlayer gaps of g-C_3N_4, leading to delamination. Similarly, NaOH treatment removes the unstable structure of g-C_3N_4, resulting in mesoporous nanosheets with an enlarged surface area.

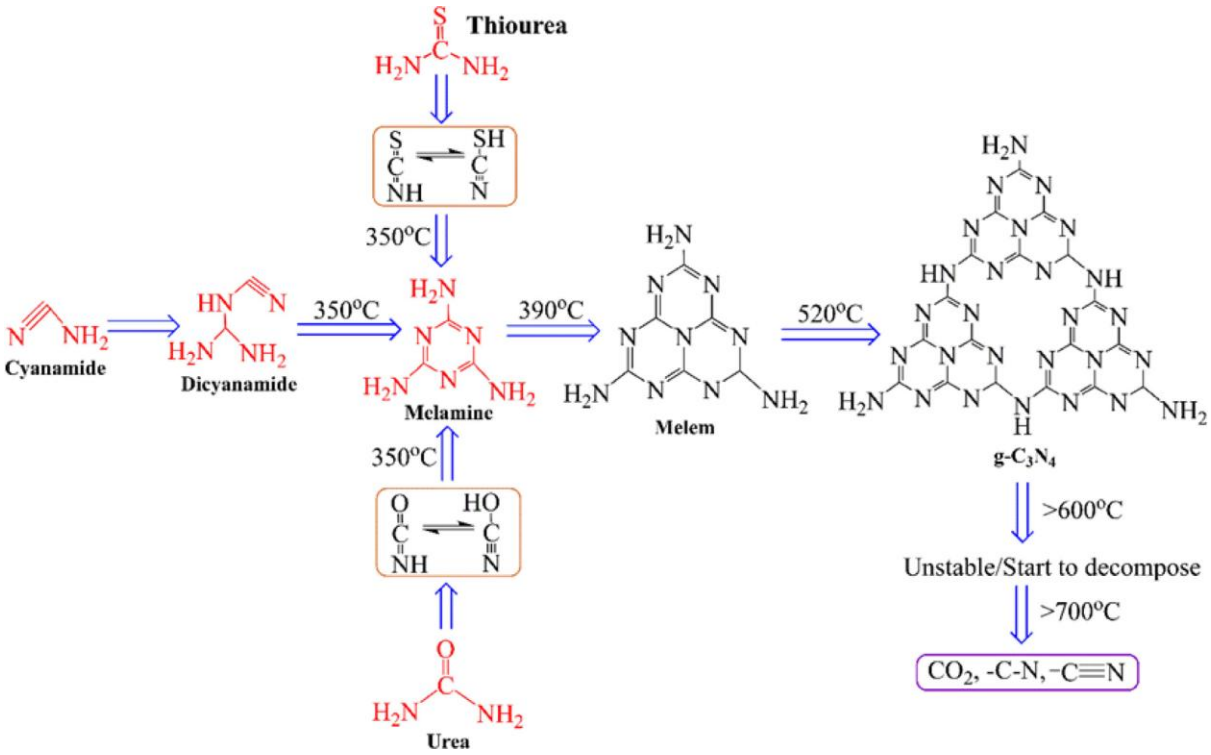

Figure 2.4. The structural transformation of the precursors varies with changes in pyrolysis temperature, where red color indicates commonly used g–C_3N_4 precursors (Wang and Wang, 2022)

2.5 Supramolecular preorganization method

The supramolecular preorganization approach does not require an external template, relying instead on molecular self-assembly to generate well-designed compositions and stable aggregate structures through non-covalent bonding (Zhou et al., 2015). Hydrogen bonds play a crucial role in forming these supramolecular aggregate structures. The

stability of these aggregates determines the final structure of the compounds. For example, coupling melamine precursors with triazine derivatives results in supramolecular preorganization (Fig. 2.3A), which is then calcined to produce g–C_3N_4 (Zhang et al., 2016).

Moreover, the supramolecular complex can be tailored through molecular design. For instance, cyanuric acid, melamine, and 2,4-diamino-6-phenyl-1,3,5-triazine form a supramolecular complex (Figure 2.3B), with its morphology dependent on the precursors' molar ratio (Zhao et al., 2019). Additionally, the cyanuric acid-melamine complex can interact with barbituric acid, urea, and caffeine to form further supramolecular complexes (J. Xu et al., 2017).

Effect of synthesis parameters

Beyond the commonly used methods, additional techniques exist for synthesizing g–C_3N_4 with varied morphologies. Chemical cleavage, which involves hydrolysis under acidic or alkaline conditions, can produce different g–C_3N_4 structures. By partially degrading the g–C_3N_4 structure and adjusting hydrolysis conditions, various morphologies can be obtained, including carbon nitride nanoleaves, nanorods, three-dimensional network carbon nitride, and nanoribbons (Zhou et al., 2015).

Microwave-assisted synthesis accelerates the polymerization of g–C_3N_4 precursors, facilitating the incorporation of π-electrons into the structure (Zhao et al., 2019; Huang et al., 2021). Recent studies have shown that microwaves can produce g–C_3N_4 with identifiable melem and its partially condensed forms, providing insights into the significance of each component in photocatalytic activity (Bian et al., 2015).

Thermal vapor condensation is another method that contributes to the synthesis of g–C_3N_4 films, which can be uniformly deposited on substrates (Xu et al., 2017). Additionally, the vapor–solid deposition approach can alter the form and structure of g–C_3N_4 (Lau et al., 2015).

Each preparation method has its advantages and limitations, allowing for the creation of diverse g–C_3N_4 morphologies with varying physicochemical properties. The intended application dictates the choice of preparation procedure, enabling the modification of g–C_3N_4's shape and structure accordingly.

3.1 Pyrolysis temperature

The structure of g–C_3N_4 polymer is greatly impacted by thermal polymerization circumstances, such as pyrolysis temperature, heating rate, solvent, and precursors. The structure of g–C_3N_4 was greatly altered by the pyrolysis temperature. Melamine–based compounds were produced by thermal polymerization of precursors at 350°C during pyrolysis (W. Ong et al., 2016). At 390°C, melamine rearranges into tris-s-triazine units. Condensation of these units forms g–C_3N_4 at 520°C. However, pyrolysis temperatures exceeding 600°C cause the polymeric g–C_3N_4 structure to become unstable and degrade. Nitrogen gas and cyano fragments are the only compounds left behind once g–C_3N_4 is entirely destroyed at temperatures more than 700°C (Xiao et. al., 2018). Figure 2.4 displays the structural conversion of the precursors as a function of temperature. As a result, to prepare g–C_3N_4, the pyrolysis temperature commonly fluctuated between 500 and 600°C.

Moreover, various structures of g–C_3N_4 might be generated by sequential pyrolysis with two separate pyrolysis temperatures as opposed to one. Melamine can be pyrolyzed at 450 degrees Celsius and then again at 300 degrees Celsius to create melem

oligomer, according to (Lau et al., 2005). Melon may be obtained at a temperature of 550 degrees Celsius.

3.2 Heating rate

The rate at which g–C_3N_4 is heated may have an impact on the rate at which the precursor polymerizes. The impact of heating rate on the structure of generated g–C_3N_4 has not yet been the topic of any investigation. However, by contrasting the characterization findings of g–C_3N_4 in the preceding investigations, the impact of the heating rate could be detected. XRD results indicated that the peak intensity of g–C_3N_4 at 13.1°, synthesized at a heating rate of 2°C/min, was below than that at 20°C/min (Zhang et al., 2019), reflecting differences in the in-plane structural packing of tri-s-triazine units. Varied heating rates during g–C_3N_4 synthesis yield distinct morphologies. Xu et al. (2013) utilized three heating rates, applying 8°C/min until the calcination temperature reached 300°C in the initial phase. After that, a heating rate of 2°C per minute was utilized until the calcination temperature reached 500°C. Ultimately, a heating rate of 1°C/min was employed till the temperature of calcination reached 550°C. In comparison to that obtained using a constant heating rate, the morphology of g–C_3N_4 formed utilizing the aforementioned different heating rates displayed bigger particles and darker brightness (Zhang et al., 2019).

3.3 Solvent

The choice of solvent significantly influences the preparation and properties of g–C_3N_4. Different solvents used in the supramolecular preorganization process can alter the intermolecular interactions within the complex, resulting in varied morphologies of g–C_3N_4. For instance, Xu et al. (2014) demonstrated that a cyanuric acid-melamine complex synthesized in water formed spherical flowers, while ethanol led to tube-like structures and chloroform produced rods. Additionally, during ultra-sonication exfoliation, the solvent's surface energy plays a crucial role. Isopropanol, with its low boiling point, is effective in delaminating g–C_3N_4, whereas N-methyl-pyrrolidone's higher boiling point may cause aggregation of the delaminated material (Yang et al., 2013). Thus, solvent selection is pivotal in tailoring the morphology and exfoliation efficiency of g–C_3N_4 for various applications.

3.4 Precursors

Various precursors have been investigated for synthesizing g-C_3N_4, significantly affecting its morphology and physicochemical properties. Studies by Dong et al. (2018) and Zhang et al. (2013) revealed that precursors such as thiourea, dicyandiamide, urea, and melamine produce distinct morphologies and microstructures, thereby influencing photocatalytic activity differently. Melamine showed superior thermal stability and yield, whereas urea-based g-C_3N_4 exhibited the highest photocatalytic performance, followed by thiourea, dicyandiamide, and melamine-based materials. Lee et al. (2017) reported varied electrochemical behaviors among precursors, with tri-thiocyanuric acid and cyanuric acid showing lower overpotentials in biomarker sensing applications. Nguyen

et al. (2021) further emphasized the contribution of different precursors to diverse g-C_3N_4 morphologies.

Moreover, subsequent exfoliation of g-C_3N_4 through chemical oxidation can yield water-dispersible forms. Among the various precursors investigated, g-C_3N_4 derived from thiourea exhibited superior photocatalytic activity, attributed to enhanced adsorption capacity and efficient charge separation mechanisms. These findings underscore the critical role of precursor selection in tailoring the properties and applications of g-C_3N_4 nanomaterials.

Modification

Modification is an effective technique to enhance the physicochemical properties of g-C_3N_4 for diverse applications. (Jiang et al., 2021). In general, the alteration of g–C_3N_4 could be separated into three groups as indicated in Figure 2.5.

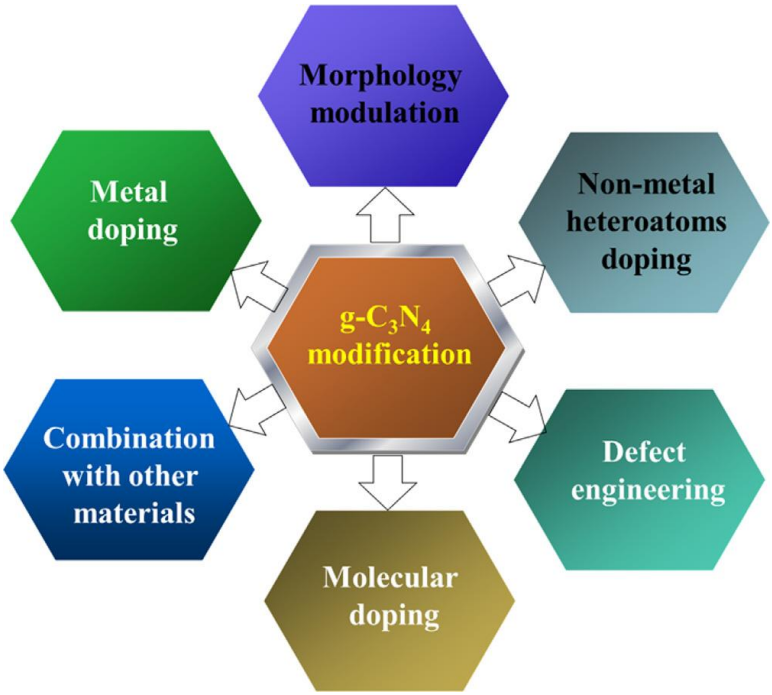

Figure 2.5. Common modification methods of g–C_3N_4 (Wang and Wang, 2022).

4.1 Non–metal heteroatoms doping

Recent studies have extensively explored non-metal heteroatoms doping as a method to modify g-C_3N_4, aiming to alter its physicochemical properties such as electron mobility and conductivity (Jiang et al., 2021). Non-metal heteroatoms for g-C_3N_4 modification include oxygen, sulfur, phosphorus, boron, fluorine, iodine, and carbon (C. Hu et al., 2019).

Furthermore, researchers have investigated the co-doping of heteroatoms in g-C_3N_4. For instance, Huang et al. (2019) synthesized phosphorus and oxygen co-doped g-C_3N_4, where phosphorus atoms substituted the corner and bay carbon sites while oxygen atoms replaced nitrogen sites. This dual doping strategy aims to synergistically enhance the material's performance by leveraging the complementary effects of different heteroatoms. The phosphorus and oxygen co–doping narrowed the

Table 2–1 Role of non–metal doping in improving the photocatalytic activity of g–C_3N_4.

Dopant	Content	Role	Application
O_2	9.9 mol%	To facilitate the separation of e^-/h^+ pairings	Evolution of H_2
O_2	8.9%	To narrow the bandgap; to facilitate the separation of e^-/h^+ couples	Removal of pollutant
O_2	4.9%	To improve adsorption capability; to modify the electrical structure	Removal of pollutant
O_2	N.A.	To modulate the electronic structure	Removal of pollutant
S	0.05% (wt)	To narrow the bandgap	Reduction of CO_2
S	0.5% (wt)	To alter the electrical structure; to facilitate the separation of e^-/h^+ couples	Removal of pollutant
B	0.7% (wt)	To increase photo–adsorption; to promote the separation of e^-/h^+ couples	Evolution of H_2
P	28% (wt)	To improve selectivity towards the related aldehyde.	Removal of pollutant
P	0.06% (wt)	To enhance the separation of e^-/h^+ pairings; to widen band gap.	Removal of pollutant
C	N.A.	To improve the visible–light absorption capability	Evolution of H_2
C	46% (wt)	To narrow band gap; to enhance the separation of e^-/h^+ couples	Removal of pollutant

I	10% (wt)	To narrow bandgap; to enhance the separation of e^-/h^+ couples	Fixation of nitrogen
F	0.7% (wt)	To enhance the separation of e^-/h^+ pairings	Removal of pollutant
S	0.33% (wt)	To facilitate the separation of e^-/h^+ couples; to produce carbon defect	Fixation of nitrogen
O_2	N.A.	To modify the p band state and long pair electrons state; to enhance the separation of e^-/h^+ couples; to produce nitrogen vacancy	Evolution of H_2

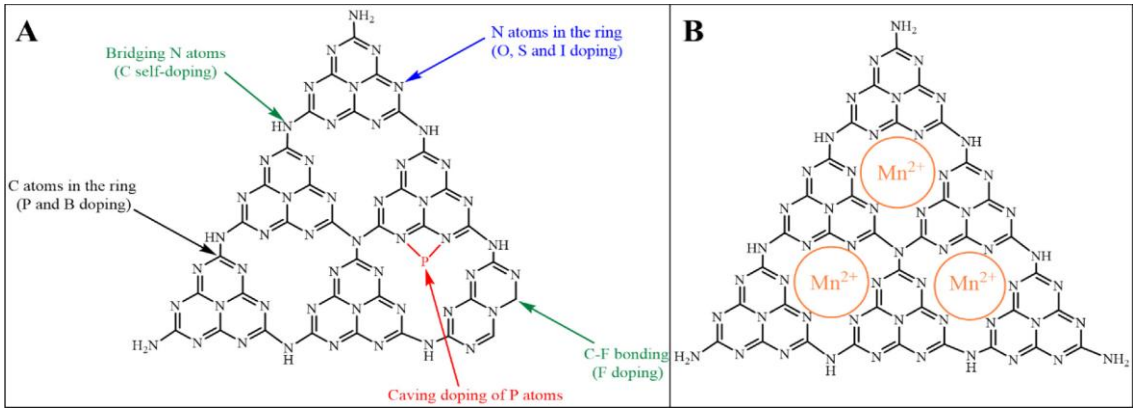

Figure 2.6 Potential sites for non-metal doping in the monolayer structure of g-C_3N_4 include (A) non-metal heteroatoms, as elucidated by Wen et al. (2017), and (B) incorporation of metal ions.

band gap, increased specific surface area, and improved charge separation. Liu et al. (2019) created g–C_3N_4 that was co-doped with sulphur and phosphorous, with the morphology of the material being modulated by the ratio of sulphur to phosphorous. Additionally, the co-doping of phosphorus and sulphur created new pathways for photogenerated electrons and holes, thereby augmenting the photocatalytic activity of g–C_3N_4. Similarly, co-doped g–C_3N_4 with boron and sulphur was also produced; this improved the photocatalytic activity of g–C_3N_4 by adjusting its electronic characteristics, inhibiting the recombination of photogenerated charge carriers, and trapping photo–induced electrons (Babu et al., 2018). Additionally, co–doping of phosphorus, sulphur, and oxygen was prepared; this attracted photoexcited electrons and greatly facilitated charge separation across the heptazine rings (Y. Chu et al., 2020). Sulphur and oxygen atoms replaced the nitrogen atoms during the synthesis process, and phosphorous atoms replaced the carbon atoms during the phosphorous, sulphur, and oxygen co–doping process. It is mentioned that defects may form as a result of heteroatom doping. The contribution of common non–metal and metal doping to enhancing g–C_3N_4's photocatalytic activity was listed in Table 2.1.

Table 2.1 makes clear that the functions of metal doping and non–metal heteroatoms are to control the bandgap of g–C_3N_4, lessen photogenerated electron and hole recombination and increase the visible light absorption region. Even though every modification has the same ultimate goal, there are differences in how well they perform, which may be related to the various dopant qualities. As an illustration, varying the doping of non–metal heteroatoms may lead to the formation of distinct structures (Figure 2.6A).

Carbon doping has the potential to replace the bridging nitrogen atoms in aromatic triazine rings, whereas oxygen, sulphur, and iodine doping can replace the nitrogen atoms in the rings (Figure 2.6A). The delocalization of the p–conjugated electrons may be encouraged by substituting the aforementioned atoms for nitrogen atoms (C. Hu et. al, 2018). On the other hand, as shown in the same figure, phosphorous and boron doping selectively replaced the carbon atoms, potentially leading to the creation of Lewis acid sites. Wei et al. (2020) demonstrated that boron doping leads to increased carrier mobility due to higher delocalization of the highest occupied molecular orbital (HOMO) and the lowest unoccupied molecular orbital (LUMO). Liu et al. (2016) found that phosphorous doping significantly reduces the intrinsic band gap and facilitates electron transfer from the valence band to the conduction band.

Fluorine doping can form carbon and fluorine bonds within the g–C3N4 structure, with fluorine atoms occupying the valence band due to their high electronegativity, thus reducing electronic band gaps (B. Zhu et al., 2017). Additionally, using monohydroamine phosphate as a phosphorous precursor may result in cave doping by phosphorous atoms (J. Ran et al., 2015).

It is observed that occasionally the g–C_3N_4 framework did not contain non–metal heteroatoms. Rather, they established surface–level functional groups. Other non–metal heteroatom–containing functional groups have not yet been found to have the ability to increase photocatalytic activity in addition to those containing oxygen. They are typically found in the

hole, as depicted in Figure 2.6B, for metal doping. However, in certain instances, they might also load onto the g–C_3N_4 surface. The photo–catalytic activity may also be enhanced by the metal ion with a surface decoration. Our earlier research showed that the surface–decorated iron oxides significantly altered the g–C_3N_4 surface charge distribution, resulting in a positive and negative region that sped up the electron transfer (Wang et al., 2020).

4.2 Metal doping

The metal ions could also be employed to change g–C_3N_4, just like non–metal heteroatoms can. It is possible to dope the huge caves of g–C_3N_4 with transition metal ions, including iron, zinc, cobalt, nickel, titanium, and copper (Deng et al., 2019). Metal doping was shown by DFT calculations to be an effective way to modify the charge distribution on the surface of g–C_3N_4, increase carrier mobility, and improve light absorption (X. Chen et al., 2019). The alkali–metal ions K^+ and Na^+ have the potential to cause an uneven spatial charge distribution in various intercalated locations, boost the concentration of free carriers, and enhance the rate of charge recombination (W. Yan et al., 2020).

Furthermore, g–C_3N_4's surface, not the cave, may potentially experience metal doping. Platinum–doped g–C_3N_4 was created by Ong et al. (W. Ong et. al., 2015), wherein platinum was deposited on the g–C_3N_4 surface. Bimetallic doping could be prepared in addition to single metal doping to increase g–C_3N_4's catalytic activity. Our earlier research has shown that g–C_3N_4 co–doped with iron and cobalt exhibited superior catalytic activity to peroxymonosulfate compared to g–C_3N_4 doped with either iron or cobalt alone (S. Wang et. al 2020). Likewise, co–doping g–C_3N_4 with platinum and nickel, iron and cerium, or iron and copper enhanced its catalytic activity (T. Pan et. al., 2020).

Recent studies have focused on single-atom transition metal doping of g–C_3N_4, which exhibits superior catalytic activity and stability compared to conventional bulk transition metal

doping due to higher utilization efficiency. Peng et al. (2022) synthesized single-atom iron-doped g–C_3N_4, demonstrating improved activation capacity towards peroxymonosulfate. Similarly, Liu et al. (2021) investigated single-atom palladium doping of g–C_3N_4, revealing enhanced photocatalytic activity towards NO.

Table 2–2 Role of metal doping in improving the photocatalytic activity of g–C_3N_4

Dopant	Content	Role	Application
Fe	0.5% (wt)	To narrow bandgap; to extend the visible light absorption region	Evolution of H_2 and removal of pollutant
Fe	1.3% (wt)	To favor the exfoliation; to create Fe–N active sites	Removal of pollutant
Fe	19.43% (wt)	To create Fe–N active sites	Removal of pollutant
Fe	1% (wt)	To create FeN_4 active sites	Removal of pollutant
Co	4.13% (wt)	To enhance adsorption capacity	Removal of pollutant
Co	2.71% (wt)	To narrow bandgap; to create Co–N active sites	Evolution of H_2 and removal of pollutant
Cu	2.71% (wt)	To create active sites	Evolution of O_2
Ni	0.5% (wt)	To increase active sites; to promote the electron transfer	Evolution of H_2 and removal of pollutant
Zn	0.4% (wt)	To narrow bandgap; to enhance the light absorption	Removal of pollutant
Pd	1.2% (wt)	To alter the electron excitation manner; to accelerate hydrogen evolution kinetics	Evolution of H2
K	7% (wt)	To promote the separation of e^- and h^+ pairs; to modulate the electronic	Reduction of CO_2

		structure; to enhance visible light absorption	
Mo	3% (wt)	To modulate the crystal growth of g–C_3N_4; to enhance adsorption capacity	Removal of pollutant
Se	0.095% (wt)	To create nitrogen vacancy; to favor the exfoliation	Removal of pollutant

Table 2.2 demonstrates the capability of oxygen-doped g-C_3N_4 to activate peroxymonosulfate (PMS) and generate diverse reactive species for the degradation of organic pollutants. This indicates that the reactive species produced during PMS activation can be influenced by preparation methods and the concentration of oxygen doping. Moreover, while iron doping results in the formation of the Fe-N configuration, the coordination and iron content in metal-doped g-C_3N_4, such as with iron, can also alter the reactive species generated. The catalytic efficiency of g-C_3N_4 can be further improved through co-doping with heteroatoms and metals, beyond the modifications induced by single heteroatoms or metals.

It has been observed that doping content is crucial. Overdoping may result in g–C_3N_4's reduced photo–catalytic activity. When it comes to metal doping, for example, overdoping may cause metal to aggregate and reduce photo–catalytic activity.

4.2.1 Alkali metal

Alkali metal ions, such as K^+ and Na^+, were integrated into the nitrogen sites of the g-C_3N_4 framework, significantly enhancing the efficiency of charge carrier transfer, transport, and separation. This modification facilitates a spatial distribution of charge carriers, thereby improving photocatalytic redox reactions. Hu et al. were the first to synthesize potassium-doped g-C_3N_4 with tunable band gaps, using dicyandiamide and potassium hydrate as precursors. They proposed that K^+ ions might coordinate with the large C-N rings. Additionally, they demonstrated that the conduction band (CB) and valence band (VB) potentials of g-C_3N_4 could be modulated by varying the K^+ concentration, enabling the formation of both •OH and $•O_2^-$, which significantly increased the photodegradation rate. Similarly, Zhang et al. developed a sodium-doped g-C_3N_4 photocatalyst with a tunable band gap using dicyandiamide and sodium hydrate as precursors, observing comparable results upon Na^+ doping.

4.2.2 Transition metal

In addition to alkali metal doping, the incorporation of other metals such as Pd, Fe, Co, Cu, W, Zn, and Zr has been extensively employed to enhance the optical and electronic properties of graphitic carbon nitride (g-C_3N_4). Metal doping effectively increases light absorption, reduces the band gap, accelerates charge mobility, and prolongs the lifetime of charge carriers, all of which are essential for significant photocatalytic activity. g-C_3N_4 readily captures metal cations due to the strong interaction between the cations and the negatively charged nitrogen atoms, which is attributed to the lone pair of electrons on the nitrogen atoms in g-C_3N_4.

Incorporation of g–C_3N_4 with other materials

Modifications to g–C_3N_4 could include incorporation of additional materials, metal doping, and doping with non–metal heteroatoms. Han et al. (2019) explored covalent (covalent bonding or π-π stacking interactions) and non-covalent modifications to enhance the coupling of g-C_3N_4 with other materials. Single–atom cobalt–doped g–C_3N_4 was found to improve surface charge separation and hydrogen peroxide production, according to Chu et al. (2020). Apart from covalent alteration, g–C_3N_4's physiochemical characteristics may also be enhanced by noncovalent treatment. The optoelectric characteristics of g–C_3N_4 were reported to be enhanced by noncovalent treatment with copper phthalocyanine by Zhao et al. (2019).

The most popular and extensively researched combination involves incorporating g–C_3N_4 with another semiconductor, which is often created by noncovalent bonding. This combination has the potential to form heterojunctions that facilitate the separation of charges spatially (J. Fu et. al., 2018). Additionally, the electron transfer may be accelerated by the heterojunction structure. Furthermore, there is a possibility to improve

the adsorption capacity. This type of incorporation could provide, in general, four heterojunction structures: the Schottky junction (Figure 2.7A), Type I (Figure.2.7B), Type II (Figure. 2.7C), and Type III (Figure. 2.7D).

The band gap differential between two materials in types I, II, and III heterojunctions dictates the direction of electron transfer. For instance, in CdS/ g–C_3N_4 combinations, electrons transfer from the g–C_3N_4 conduction band to CdS, whereas in CdS quantum dot/ g–C_3N_4 configurations, electrons transfer from the CdS quantum dot conduction band to g–C_3N_4 (Wen et al., 2017). The synergistic potential of g–C_3N_4 with other materials is assessed based on their band gap alignment. Schottky junctions and Type II heterojunctions, which significantly enhance photocatalytic activity, rely on this band gap alignment (Thomas et al., 2008). Various semiconductors such as Cu_2O, TiO_2, ZnO, WO_3, BiOX, Bi_2WO_6, Fe_2O_3, CdS, $BiVO_4$, Ag_3PO_4, In_2O_3, CeO_2, and SnO_2 are employed to form these heterojunctions (Paul et al., 2020). These combinations exploit the band gap differences to promote efficient charge separation and transfer, crucial for enhancing the photocatalytic capabilities of the resulting heterojunctions.

Hybrid materials of g–C_3N_4 and carbonaceous components can be formed to achieve several advantages: promoting charge separation, enhancing active sites and adsorption capabilities, adjusting band gap properties, and improving conductivity. Commonly utilized carbonaceous materials include carbon nanotubes, graphene, carbon quantum dots, carbon fibers, activated carbon, carbon black, and biochar (Bie et al., 2021). Chen et al. (2020) demonstrated enhanced photocatalytic activity by covalently bonding oxygen-doped g–C_3N_4 with -NHx groups from g–C_3N_4 surface, creating oxygen-doped carbon nitride/graphitic carbon nitride hybrids. Recent studies have also shown that incorporating g–C_3N_4 into biochar through noncovalent interactions enhances catalytic activity for peroxymonosulfate (Wang et al., 2022). These hybrid materials

leverage the unique properties of both g-C_3N_4 and carbonaceous materials to improve their performance in various applications, particularly in photocatalysis and environmental remediation.

5.1 Morphology modulation

The morphology of g–C3N_4 significantly influences its physicochemical properties, prompting numerous studies to explore methods for controlling its preparation and modifying its structure. Reported forms of g–C_3N_4 include 0-dimensional (e.g., g–C_3N_4 quantum dots), 1-dimensional (e.g., g–C_3N_4 tubes), 2-dimensional (e.g., g–C_3N_4 nanosheets), and 3-dimensional structures (e.g., nanoporous g–C_3N_4 microspheres) (Bandhopadhyay et al., 2017). These categories reflect the diverse approaches employed to tailor the morphology of g-C_3N_4, aiming to optimize its performance in various applications such as photocatalysis and sensing.

5.2 Molecular doping

Molecular doping of g-C_3N_4 involves structural adjustments during or after precursor polymerization (Cao et al., 2015). Xia et al. (2017) developed hierarchical g-C_3N_4 nanosheets with amine functional groups, demonstrating enhanced photocatalytic CO_2 reduction compared to conventional g-C_3N_4. Chu et al. (2020) modified g-C_3N_4 with anthraquinone to improve reduction selectivity, while Zeng et al. (2020) grafted cationic polyethyleneimine (PEI) molecules onto g-C_3N_4, enhancing photocatalytic H_2O_2 production. Additionally, dye molecules can be immobilized onto g-C_3N_4 surfaces through chemical or physical interactions

expanding the excitation wavelength response rang further improving the photocatalytic activity of g–C_3N_4 (J. Fu et. al., 2018). Common dye molecules include *Eosin Y*, *Rose Bengal* and *Fluorescein* (Z. Jiang et. al., 20184).

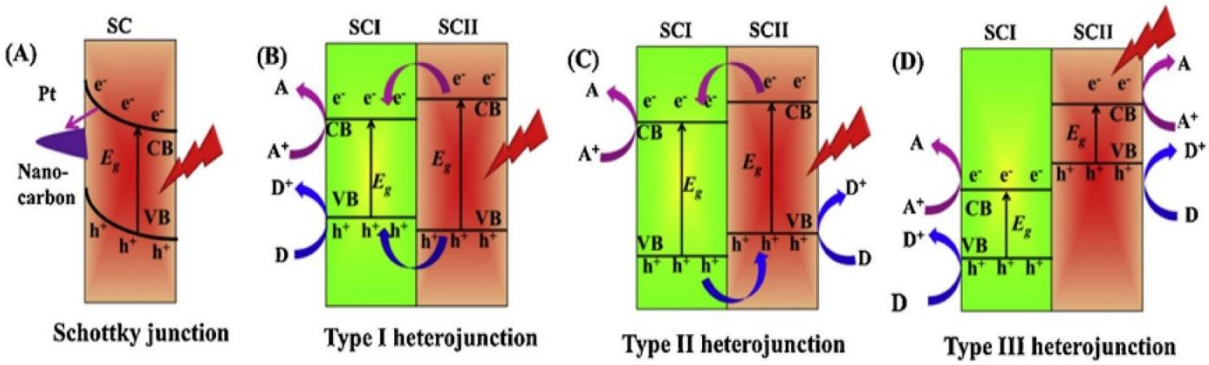

Figure 2.7. Spatial charge–separation mechanisms for four different types of semiconductor heterojunctions: (A) Schottky junction, (B) Type I, (C) Type II, and (D) Type III

In addition to dye molecules, a variety of other substances have been employed to modify graphitic carbon nitride (g-C_3N_4). Lau et al. (2015) synthesized g-C_3N_4 modified with urea, which facilitated interactions between metal and support with platinum co-catalysts, thereby enhancing interfacial charge transfer at hydrogen evolution sites. Zhang et al. (2014) introduced pyrrole modifications to g-C_3N_4, which improved carrier migration and separation efficiency under visible light. Tang et al. (2019) reported on oxamide-modified g-C_3N_4, which shifted the light absorption edge to 650 nm and accelerated charge carrier dynamics.

These molecular modifications illustrate diverse strategies to tailor g-C_3N_4 properties for enhanced performance in photocatalytic applications, emphasizing the importance of molecular design in achieving specific functional enhancements.

5.3 Defect engineering

Defect engineering is a valuable approach for modifying the electronic structure and surface characteristics of g-C_3N_4 to achieve desired physicochemical properties.

Thermal treatments in oxidizing or reducing environments are commonly employed to introduce vacancies into g-C_3N_4, altering its defect landscape. Various types of defects include vacancies (point defects), interstitials, dislocations (line defects), and voids (bulk defects), each impacting material properties differently. Carbon and nitrogen vacancies can be induced by specific gas environments such as carbon dioxide and hydrogen, respectively (Han et al., 2019; Hu et al., 2014). Oxygen vacancies may result from combining g-C_3N_4 with metal oxides like TiO_2 and BiOCl. Additionally, defect engineering techniques involving photoassisted heating or precursor isomerization have been utilized to create holey structures and cyanamide defects in g-C_3N_4 (Shi et al.; Yuan et al.). These engineered defect sites have demonstrated enhancements in charge separation efficiency and photocatalytic performance of g-C_3N_4.

Environment applications

Owing to its special qualities, which include a moderate energy gap, superior electronic properties, a large number of functional groups, and surface defects, g–C_3N_4 can be used for a variety of environmental applications, such as photocatalysis, Fenton–like catalysts, adsorbents, membranes, and photocatalysis. The g–C_3N_4 environmental applications mentioned above will be highlighted in this section.

6.1 Photocatalyst

g-C_3N_4 exhibits notable photocatalytic activity, making it suitable for various applications as a photocatalyst. Specifically, g-C_3N_4 has been utilized in hydrogen production through photocatalytic water splitting. Additionally, it has shown effectiveness in NOx removal, degradation of organic pollutants in wastewater, and CO_2 conversion processes. These applications leverage g-C_3N_4's ability to absorb light and

generate charge carriers that drive redox reactions, highlighting its potential contribution to sustainable energy and environmental remediation technologies.

6.2 Water splitting

In addition to dye molecules, a variety of other substances have been employed to modify graphitic carbon nitride (g-C_3N_4). Lau et al. (2015) synthesized g-C_3N_4 modified with urea, which facilitated interactions between metal and support with platinum co-catalysts, thereby enhancing interfacial charge transfer at hydrogen evolution sites. Zhang et al. (2014) introduced pyrrole modifications to g-C_3N_4, which improved carrier migration and separation efficiency under visible light. Tang et al. (2019) reported on oxamide-modified g-C_3N_4, which shifted the light absorption edge to 650 nm and accelerated charge carrier dynamics.

The conversion of solar energy into chemical energy stored in hydrogen via solar water splitting presents a promising solution to the global energy crisis. This process involves two half-reactions: water oxidation to produce oxygen gas and water reduction to produce hydrogen gas, both driven by electron transfer. Semiconductor materials like g-C_3N_4 can generate electrons under visible light irradiation, crucial for initiating these reactions. However, pristine g-C_3N_4 faces challenges such as low surface area and rapid charge recombination, limiting its efficiency in water splitting.

To enhance the photocatalytic activity of g-C_3N_4, various strategies have been explored. Chen et al. (2019) demonstrated improved water splitting efficiency by using three-dimensional porous g-C_3N_4, achieving significantly higher rates of H_2 and O_2 evolution compared to pristine g-C_3N_4. Lin et al. (2020) reported that sulfur-doped g-C_3N_4 exhibited superior performance in water splitting, achieving high rates of H_2 and O_2 evolution. Moreover, the incorporation of g-C_3N_4 with other materials, such as MnOx/g-

C_3N_4/CdS/Pt, significantly enhanced the evolution rates of H_2 and O_2 under visible light irradiation (Pan et al., 2021).

These advancements highlight the versatility of g-C_3N_4 in photocatalytic applications and underscore the importance of tailored modifications to optimize its performance for efficient solar-driven water splitting.

6.3 NO_x removal

It is efficient to convert NOx from the air to particulate–phase nitrate. Thus, there has been a lot of interest lately in photocatalytic NOx removal under ambient settings. When exposed to oxygen and visible light, g–C_3N_4 as a photo–catalyst can generate superoxide and electron hole (h^+) radicals, which can be utilised to eliminate NOx. However, because virgin g–C_3N_4 lacked redundant coordination bonds and defect states in its electronic structure, as well as having a low adsorption ability to NOx, it demonstrated a low removal capacity to NOx (Z. Hong et. al., 2013). Wang et al.'s regulation of the nitrogen vacancy enhanced the porous g–C_3N_4's ability to remove NOx (Z. Wang et. al., 2019). In addition to providing the active sites for reactant adsorption activation and photo–induced electron capture, the nitrogen vacancy improved g–C_3N_4's ability to absorb light. Lin et al synthesized S–g–C_3N_4, which is sulfur–doped g–C_3N_4 (Y. Lin et. al., 2020) The visible light response was enhanced by the g–C_3N_4 band gap being expanded to 2.94 eV due to sulphur doping, which also produced an electron capture centre that reduced charge recombination. S–g–C_3N_4 on the other hand shown a greater ability to adsorb O_2. The aforementioned explanations explain why S–g–C_3N_4 shown an improved ability to remove NOx.

Metal oxide-doped g-C_3N_4, aside from non-metal heteroatom doping, has shown enhanced capability for NOx removal. Liu et al. (2020) synthesized BiOBr-doped g-C_3N_4, achieving 63% NO elimination (initial concentration 0.6 mg/L) with 96% selectivity for

carbonaceous products. The heterojunction formed between BiOBr and g-C_3N_4 facilitated the generation of reactive species and established a spatially conductive network, enhancing NOx removal efficiency. Additionally, the addition of reduced graphene oxide to g-C_3N_4 increased its surface area and reduced the recombination of photogenerated charges (Gu et al., 2020), potentially further enhancing g-C_3N_4's NOx removal capacity. These modifications illustrate effective strategies to tailor g-C_3N_4 for improved environmental remediation applications, highlighting the importance of heterojunction formation and surface area enhancement in enhancing photocatalytic performance.

6.4 CO_2 conversion

A promising approach to address global greenhouse gas emissions and energy shortages is the photocatalytic conversion of CO_2 into carbon-based fuels (Jiao et al., 2020). However, pristine g-C_3N_4 suffers from significant electron-hole recombination, limiting CO_2 photo-reduction efficiency. Fu et al. introduced oxygen doping into g-C_3N_4, resulting in a narrower bandgap, enhanced CO_2 affinity, and increased light absorption capacity compared to pristine g-C_3N_4 (Lin et al., 2020). Oxygen doping also improved the separation efficiency of photogenerated charge carriers, thereby enhancing the overall performance of g-C_3N_4 in CO_2 conversion applications. These advancements highlight the importance of modifying g-C_3N_4 to optimize its photocatalytic properties for efficient CO_2 utilization and renewable fuel production. According to Wang et al, potassium doping can result in interlayer doping that suppresses photo–induced electron and hole recombination, hence improving CO_2 photo–reduction (J. Pan et. al., 2021). Z–scheme a–Fe_2O_3/g–C_3N_4 composite was created by Jiang et al. and shown improved CO_2 reduction over pure g–C_3N_4 (K. Li et. al., 2015). The increased adsorption and decreased electron and electron hole recombination were the causes of the increased photo–reduction

capability. Cheng et al. synthesized porous few–layer g–C_3N_4 from the bottom up and coordinated single–atomic–site Ni to create single–atom Ni–doped g–C_3N_4 (L. Cheng et. al., 2020). The superiority in interfacial carrier transfer and synergistic N–Ni–N connection was driven by the Ni–N doping intercalation. Furthermore, the Ni–N coordination binds to CO_2 favorably, which increases the CO_2 reduction even more.

6.5 Treatment of emerging contaminants in wastewater

The removal of emerging contaminants (ECs) from water and wastewater has emerged as a critical research area, driven by environmental concerns and public health considerations (Wang et al., 2020). Photocatalytic processes utilizing semiconductors like g-C_3N_4 have shown promise in degrading various pollutants, including organic pollutants and heavy metals, through the generation of photo-induced electrons and holes (Pelizzetti and Minero, 1993). However, pristine g-C_3N_4 is hindered by rapid charge recombination, limiting its effectiveness in pollutant removal. Consequently, significant efforts have been directed towards enhancing its photocatalytic activity to improve pollutant removal efficiencies (Liu et al., 2020).

Mesoporous g-C_3N_4, as reported by Dou et al. (2020), exhibited superior performance in the removal of antibiotics under visible light, highlighting the benefits of enhanced surface area and improved light absorption. Tao et al. (2019) synthesized TiO_2/g-C_3N_4 composites that demonstrated enhanced capability in removing Rhodamine B due to efficient separation of photo-induced charge carriers. Similarly, Renukumari and Jeyakumari (2020) developed $ZnFe_2O_4$/g-C_3N_4 composites, which showed high removal capacity for Rhodamine B attributed to effective charge separation.

Furthermore, doping g-C_3N_4 with carbon quantum dots has been shown to significantly enhance its photocatalytic activity, leading to improved removal of organic

pollutants (Ai et al., 2021). Recent studies have also explored heterojunctions like $WO_3/MoO_3/g\text{-}C_3N_4$, demonstrating superior reduction capacity for bicarbonate and Cr(VI) (Huang et al., 2021), and $CeO_2/g\text{-}C_3N_4/V_2O_5$ systems with enhanced reduction capabilities (Kumar et al., 2020).

In addition to semiconductor modifications, the use of oxidants such as H_2O_2 and persulfate has been integrated with $g\text{-}C_3N_4$ photocatalysis to enhance pollutant removal. Cui et al. (2012) reported that $g\text{-}C_3N_4$ can activate H_2O_2 to degrade Rhodamine B effectively, surpassing the performance of the single $g\text{-}C_3N_4$ system. Similarly, Song et al. (2020) demonstrated synergistic effects between $g\text{-}C_3N_4$ and persulfate for sulfamethoxazole removal, where sulfate radicals and holes played crucial roles in degradation.

Overall, the modification of $g\text{-}C_3N_4$ through doping and heterojunction formation, coupled with the use of oxidants, represents a promising approach to enhance its photocatalytic efficiency for the removal of diverse emerging contaminants from water and wastewater. Continued research in this area is crucial for developing sustainable water treatment technologies to mitigate environmental pollution and ensure safe water resources for future generations.

6.6 Fenton–like catalysts

The Fenton reaction has been extensively utilized for the degradation of persistent organic pollutants, employing various Fenton-like catalysts. $g\text{-}C_3N_4$ has emerged as a potential Fenton-like catalyst capable of activating hydrogen peroxide (H_2O_2) and persulfate species such as peroxymonosulfate and peroxydisulfate under visible light absence conditions. Zhu et al. demonstrated that $g\text{-}C_3N_4$ activates H_2O_2 for the

degradation of Rhodamine B, although its catalytic activity in its pristine form is limited, necessitating extensive modification (Zhu et al., 2020). Studies have explored the modification of g-C_3N_4 to enhance its catalytic activity. Zhang et al. found that cobalt doping improved g-C_3N_4's activity towards H_2O_2 and peroxymonosulfate (Yang et al., 2021). Oxygen-doped g-C_3N_4 also exhibited enhanced catalytic activity towards peroxymonosulfate due to electron distribution modulation caused by oxygen doping. Moreover, exfoliation of oxygen-doped g-C_3N_4 further increased its catalytic activity by exposing more active sites (Liu et al., 2019).

Pd-doped g-C_3N_4 was reported by Wang et al. to enhance catalytic activity towards peroxymonosulfate, leveraging Pd's ability to promote H_2O_2 activation derived from peroxymonosulfate-water reactions (Wang et al., 2009). Similarly, iron doping altered g-C_3N_4's catalytic mechanism depending on the iron species present; iron oxides/g-C_3N_4 activated peroxymonosulfate to produce radicals, while Fe(III)/g-C_3N_4 generated non-radicals (Chen et al., 2019).

Bimetallic doping, as shown in recent studies, further enhances g-C_3N_4's catalytic activity. For instance, Fe-Co-O co-doped g-C_3N_4 exhibited superior peroxymonosulfate activation compared to single g-C_3N_4 and iron oxides/g-C_3N_4 (Wang et al., 2020). Additionally, integrating g-C_3N_4 with other materials, such as biochar, has been shown to enhance catalytic activity towards peroxymonosulfate (Jiang et al., 2018), although the specific synergistic mechanisms vary depending on the materials involved.

Modifying g-C_3N_4 through doping and composite formation significantly enhances its efficacy as a Fenton-like catalyst for pollutant degradation, thereby offering potential applications in environmental remediation and wastewater treatment technologies. Further research is warranted to optimize these materials and understand their mechanisms for improved pollutant removal efficiency.

6.7 Adsorbents

Adsorption technology remains a cornerstone for the removal of diverse pollutants from water systems, encompassing heavy metal ions, pharmaceuticals, and personal care products (PPCPs), among others. Various adsorbents, including metal–organic frameworks (MOFs), covalent organic frameworks (COFs), chitosan-based materials, porous coordination polymers, and carbon-based materials, have been extensively investigated in this context. Among these, g-C_3N_4 has emerged as a promising adsorbent due to its unique structure featuring cavities and nitrogen-containing binding sites that facilitate effective pollutant adsorption (Hu et al., 2014; Xu et al., 2015; Zhang et al., 2011; Fu et al., 2019; Babu et al., 2018).

For instance, Shen demonstrated that g-C_3N_4 effectively adsorbs Cu(II), Pb(II), Cd(II), and Ni(II) ions through inner-sphere surface complexation mechanisms, achieving sorption capacities of 134 mg/g, 286 mg/g, 112 mg/g, and 41 mg/g, respectively (Jiang et al., 2018). Additionally, g-C_3N_4 has been reported to adsorb Eu(III), La(III), Nd(III), and Th(IV) ions with capacities ranging from 122.3 mg/g to 185.6 mg/g (Jo et al., 2017).

Modification strategies aimed at enhancing the adsorption capacity and selectivity of g-C_3N_4 have been explored extensively. For example, doping g-C_3N_4 with Fe_3O_4 improved its selectivity towards Zn(II), Pd(II), and Cd(II) ions by facilitating conjugation between Fe_3O_4/g-C_3N_4 and these heavy metal ions (Guo et al., 2018). Furthermore, ternary composites such as Fe_3O_4/g-C_3N_4/carbon layers have been developed to synergistically enhance the adsorption of Cr(VI) through mechanisms involving ion exchange, reduction, and complexation, achieving an impressive adsorption capacity of 50.09 mg/g (Jo et al., 2017).

In addition to heavy metal ions, g-C_3N_4 has shown promise in adsorbing organic pollutants. While pristine g-C_3N_4 typically exhibits modest adsorption capacity towards organic pollutants, the incorporation of g-C_3N_4 with carbonaceous materials has been demonstrated to enhance adsorption efficiency significantly. For example, g-C_3N_4/carbon nanotube composites exhibited enhanced adsorption of Rhodamine B compared to pristine g-C_3N_4 alone (Liu et al., 2021). Similarly, incorporating g-C_3N_4 with biochar enhanced its adsorption capacity for sulfamethoxazole compared to using biochar or g-C_3N_4 alone (Ji et al., 2017). However, some studies indicate that the synergistic effect between g-C_3N_4 and carbon nanotubes may not always lead to enhanced adsorption capacities for organic pollutants (Liu et al., 2021).

In conclusion, g-C_3N_4 holds significant potential as an adsorbent for both heavy metal ions and organic pollutants, with ongoing research focused on optimizing its properties through various modifications and composite formations to meet the demands of efficient water treatment and environmental remediation applications. Further investigation is warranted to explore new materials and innovative strategies to enhance the performance of g-C_3N_4-based adsorbents in real-world scenarios.

6.8 Membrane materials

Membrane materials are integral to the membrane separation process. Graphitic carbon nitride (g–C_3N_4)–based materials have garnered attention as potential membranes due to their triangular nanopores, which facilitate the passage of water molecules. The combination of catalytic activity and adsorption capacity of g–C_3N_4 renders it suitable for various environmental applications. Modifying g–C_3N_4 can further enhance these properties. For instance, Qu et al. developed an O–g–C_3N_4/graphene oxide/nitrogen-doped carbon nanotube membrane that exhibited remarkable tetracycline removal

efficiency under visible light (Y. Zhao et al., 2018). The membrane demonstrated consistent performance across three consecutive experiments, indicating high stability. Similarly, Chen et al. fabricated Mn_3O_4 nanodots-loaded g–C_3N_4 nanosheets, which showed superior catalytic activity and stability for peroxymonosulfate activation in organic pollutant removal (W. Zou et al., 2017). To date, various g–C_3N_4–based membranes have been developed for applications in water purification, water splitting, and CO_2 conversion, primarily leveraging the photocatalytic properties of g–C_3N_4.

6.9 Disinfectants

Graphitic carbon nitride (g–C_3N_4) is notable for its high stability and controllable band gap, making it a promising candidate for biomedical applications, particularly as an antibacterial agent. Thurston et al. demonstrated that g–C_3N_4 effectively eradicates Escherichia coli and Staphylococcus aureus under visible light. The antibacterial efficacy of g–C_3N_4 can be significantly enhanced by the incorporation of Ag nanoparticles, as evidenced by S. Wang et al. (2022), who reported that Ag-doped g–C_3N_4 efficiently deactivates E. coli, S. aureus, and Pseudomonas aeruginosa under visible light. Additionally, A. Bandyopadhyay et al. (2017) showed that a graphene/g–C_3N_4 composite killed 97.9% of E. coli after 120 minutes of visible light exposure. Carvalho et al. (2018) further noted that moderate carbon doping enhances the antibacterial properties of g–C3N4. ZnO nanoparticles (NPs) also exhibit potent antibacterial activity due to their unique physicochemical properties and photocatalytic capabilities (L. Zhou et al., 2020). Consequently, the ZnO/g–C_3N_4 composite demonstrates exceptional antibacterial activity against both gram-negative and gram-positive bacteria, with metal-doped variants further improving this efficacy (G. Zhang et al., 2014; P. Xia et al., 2017).

Steps of g–C_3N_4 as photocatalyst, adsorbent and disinfectant

Graphitic carbon nitride (g–C_3N_4) serves as a photocatalyst, adsorbent, and disinfectant primarily due to three key properties: (1) the generation of photo-induced electrons (e^-) and holes (h^+) under visible light (as illustrated in Figure 2.8), (2) the presence of surface functional groups, and (3) its unique structure. Photo-generated electrons exhibit strong reducing capabilities, enabling applications in water and heavy metal reduction and H_2O_2 activation. Conversely, photo-generated holes possess strong oxidizing properties, useful in the oxidation of organic pollutants and water. Both e^- and h^+ negatively impact bacteria and viruses, making g–C_3N_4 an effective disinfectant.

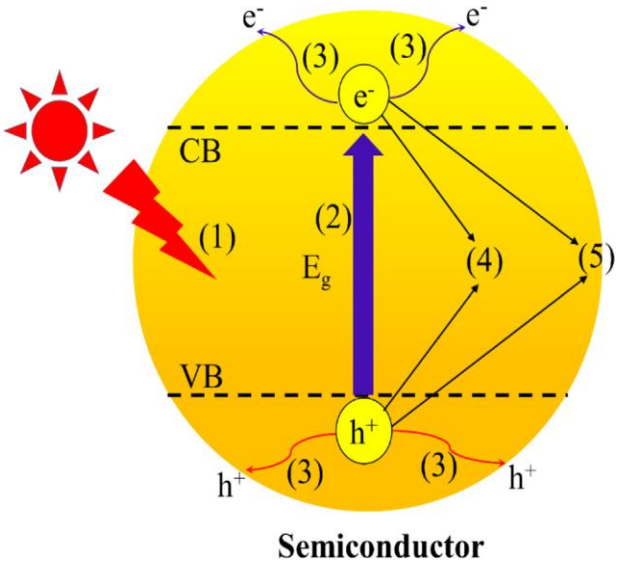

Figure 2.8. Fundamental mechanism of heterogeneous photocatalysis (1) light harvesting; (2) charge excitation; (3) charge separation and transfer; (4) bulk charge

Photo-generated electrons can activate chemical oxidants, leading to the formation of radicals such as H_2O_2 and persulfate. Surface functional groups, such as pyridinic–N, and defect sites also serve as active sites for chemical oxidation activation. The catalytic activity of g–C_3N_4 increases with the degree of defectiveness up to a certain point; beyond this, structural destruction leads to decreased activity. Surface functional groups,

including C–N, C=N, –NH–, and $–NH_2$, play crucial roles in adsorbing heavy metal ions like Cu^{2+}, Zn^{2+}, and Pb^{2+} (X. Zeng et al., 2020). Additionally, the unique structure of g–C_3N_4, characterized by tris–triazine units and a 2D lamellar architecture, enhances pollutant adsorption. Density Functional Theory (DFT) calculations have shown that heavy metal ions trapped within the holes surrounded by triazine molecules can form both three-coordinated and six-coordinated structures (Figure 2.9) (X. Zeng et al., 2020). Overall, g–C_3N_4 adsorbs heavy metal ions through electrostatic attraction, ion exchange, reduction, and complexation mechanisms.

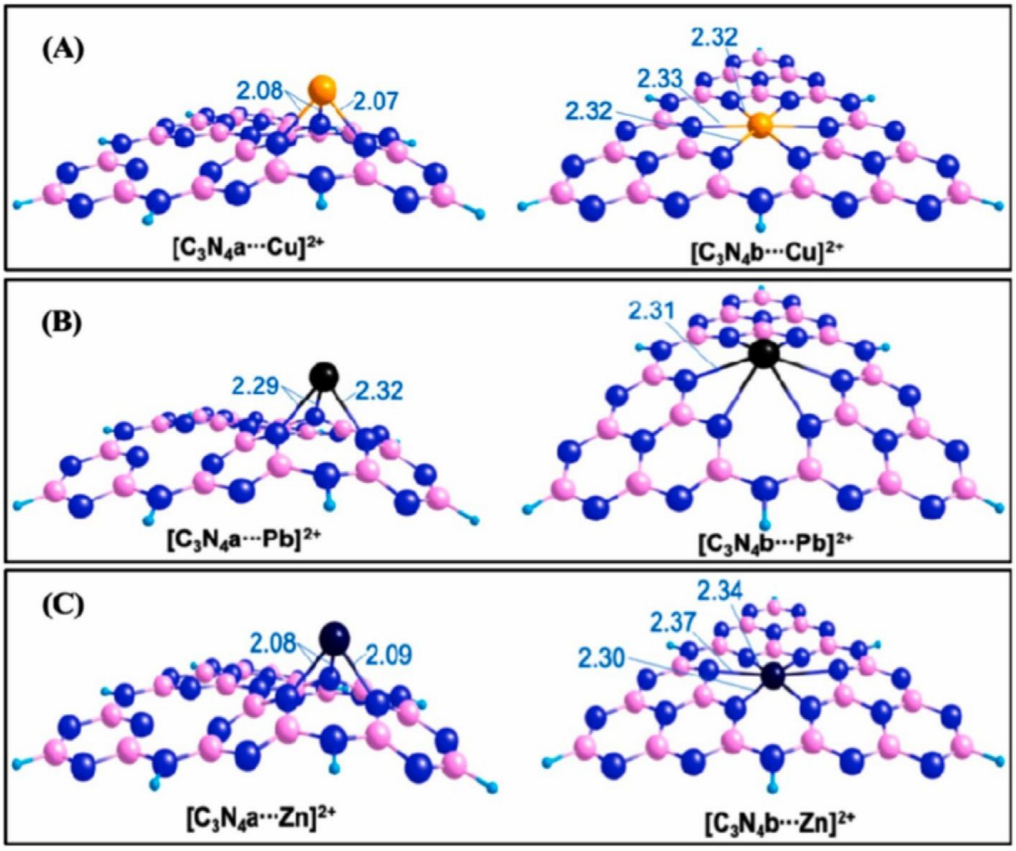

Figure 2.9. The structural model of Cu (A), Pb (B), and Zn (C) adsorption on C_3N_4 via three coordination and six coordination (Dong et al. 2021).